Nanoscale

PAPER

View Article Online
View Journal | View Issue

Cite this: *Nanoscale*, 2023, **15**, 4033

Chalcogen (S, Se, and Te) decorated few-layered $Ti_3C_2T_x$ MXene hybrids: modulation of properties through covalent bonding†

Jalal Azadmanjiri,* Pradip Kumar Roy, Lukáš Děkanovský and Zdeněk Sofer *

2D carbides and nitrides of transition metals (MXenes) have shown great promise in a variety of energy storage and energy conversion applications. The extraordinary properties of MXenes are because of their excellent conductivity, large carrier concentration, vast specific surface area, superior hydrophilicity, high volumetric capacitance, and rich surface chemistry. However, it is still desired to synthesize MXenes with specific functional groups that deliver the required characteristics. This is due to the fact that a considerable amount of metal atoms is exposed on the surface of MXenes during their synthesis through an etching procedure; hence, other anions and cations are uncontrollably implanted on their surfaces. Because of this situation, the first invented $Ti_3C_2T_x$ MXene suffers from low photoresponsivity and detectivity, large overpotential, and small sensitivity in photoelectrochemical (PEC) photodetectors, hydrogen evolution reaction (HER), and sensing applications. Therefore, surface modification of the MXene structure is required to develop the device's performance. On the other hand, there is still a lack of understanding of the MXene mechanism in such cutting-edge applications. Thus, the manipulations of MXenes are highly dependent on understanding the device mechanism, suitable modification elements, and modification methods. This study for the first time reveals the conjugation effect of pre-selected S, Se, and Te chalcogen elements on a few-layered $Ti_3C_2T_x$ MXene to synthesize new composites for PEC photodetector, HER, and vapor sensor applications. Also, the mechanism of the chalcogen decorated few-layered $Ti_3C_2T_x$ MXene composites for each application is discussed. The selection of a few-layered $Ti_3C_2T_x$ MXene is due to its fascinating characteristics which make it capable to be considered as an appropriate substrate and incorporating chalcogen atoms. The Te-decorated few-layered $Ti_3C_2T_x$ MXene composite provides better performances in PEC photodetector and vapor sensing applications. Although the potential value of the Se-decorated few-layered $Ti_3C_2T_x$ composite is slightly lower than that of the Te-decorated sample in HER application, its overpotential is still greater than that of the Te-decorated sample. The acquired results show that the S-decorated few-layered $Ti_3C_2T_x$ composite demonstrates the lowest performance in all three examined applications in comparison with the other two samples.

Received 15th October 2022,
Accepted 4th January 2023

DOI: 10.1039/d2nr05730a

rsc.li/nanoscale

1. Introduction

High-efficiency photodetectors, electrocatalysts, sensors, and many more other state-of-the-art devices, require robust nanostructures that overcome the current limitations of those instruments. Two-dimensional (2D) nanomaterials are capable of providing unique properties because of their attractive physical (*i.e.*, electrical- and photo-conductivity), chemical (*i.e.*, catalytic activity), and mechanical (*i.e.*, high stability) properties.[1–6] These fascinating characteristics of 2D nanomaterials are due to their ultrathin planar structures which result in strong quantum confinement and their large surface area.[7–9] Among the different varieties of invented and synthesized 2D nanomaterials, transition-metal carbides and carbonitrides (MXenes) have demonstrated admirable performances because of their wide specific surface area, and tendency to be bonded covalently with guest atoms because of the inner metal vacancies which are generated during their synthesis.[10–12] In addition to these, the high electrical conductivity, tunable bandgap, and great mechanical stability of MXenes make them suitable candidates for energy storage and conversion without decomposition of the structure.[13–16]

Four molecular structures of M_2X, M_3X_2, M_4X_3, and M_5C_4 MXene nanosheets (M and X stand for transition metal elements, and C or N elements, respectively) have been made accessible so far with single-, few- and multi-layer structures,[17]

Department of Inorganic Chemistry, University of Chemistry and Technology Prague, Technická 5, 166 28 Prague 6, Czech Republic. E-mail: jalal_azad2000@yahoo.com, jalal.azadmanjiri@vscht.cz, zdenek.sofer@vscht.cz

† Electronic supplementary information (ESI) available. See DOI: https://doi.org/10.1039/d2nr05730a

and the sizes of a few micrometers to the recently achieved ultra-large flakes.[18] Surface termination species (T_x) or intercalated compounds (ICs) are replaced with the "A" atoms as a result of the A-layer selective etching from the initial MAX phase. The resulting MXenes have a chemical formula of $M_{n+1}X_nT_x$ or $M_{n+1}X_nT_x$-IC after the substitution of the end groups by the intercalation.[19] T_x and ICs could be =O, –H, –OH, or –F, and NH^{4+} or NH_3 groups depending on the etchant employed and the etching process parameters (*i.e.*, etching time, etching temperature, *etc.*).[20–22] In addition, the hydrophilicity of MXene nanosheets is discovered to be caused by these functional groups of T_x and ICs.[21] Furthermore, the nature of MXenes is capable of being changed by its functional groups. For instance, the full functionalization of $Ti_3C_2T_x$ MXenes with =O can turn the metallic nature of the MXenes into a semiconductor state with a significant Seebeck coefficient.[23]

It has been investigated as a benchmark that the $Ti_3C_2T_x$ MXene has shown promising performance in energy storage and conversion. However, despite its high electronic conductivity and excellent performance in comparable electrolytic systems, it does not function well in some applications such as self-powered photoelectrochemical (PEC) photodetectors, hydrogen evolution reaction (HER) electrocatalysis, and vapor sensing applications. For instance, terminated $Ti_3C_2T_x$ MXenes have shown a large overpotential for the HER in aqueous electrolytes despite being predicted to be active in that application.[24,25] In this regard, significant efforts are required to first understand the underlying mechanisms behind the low performance of $Ti_3C_2T_x$ MXenes, and then, attempt to develop the efficiency of the MXenes with appropriate approaches like promoting charge transfer, H^+/e^- couplings, and surface catalytically active sites in such applications.

Herein, we report a solid-state annealing strategy to investigate the decorating effect of the pre-selected chalcogen (S, Se, and Te) atoms on the performance of few-layered $Ti_3C_2T_x$ MXenes in the aforementioned applications, as well as explain their mechanisms. This will reveal information about the active sites and how the distribution of electrons varies under reactional conditions. The PEC photodetector, HER, and vapor sensing working mechanisms of blank and chalcogen decorated few-layered $Ti_3C_2T_x$ MXenes with S, Se, and Te elements are yet unclear and to the best of our knowledge, there are no published studies to explain those systems. This lack of studies can partially be attributed to the undesirable $Ti_3C_2T_x$ MXene with low charge transfer and large overpotential. Thus, this work provides insight into modifications and conditions to enable improvement of the deficiencies through structural analyses. The chalcogen elements as a decoration agent have been chosen due to their high electronegativity, rich d-electron, large dipole atomic polarizability, high photoconductivity, and high responsivity characteristics.[26–28]

2. Experimental methods

2.1. Sample preparation

2.1.1. Synthesis of few-layered $Ti_3C_2T_x$ MXenes. The few-layered $Ti_3C_2T_x$ MXene was synthesized based on a previously reported research study (Scheme 1a–c).[29] To do so, 10 g of as-

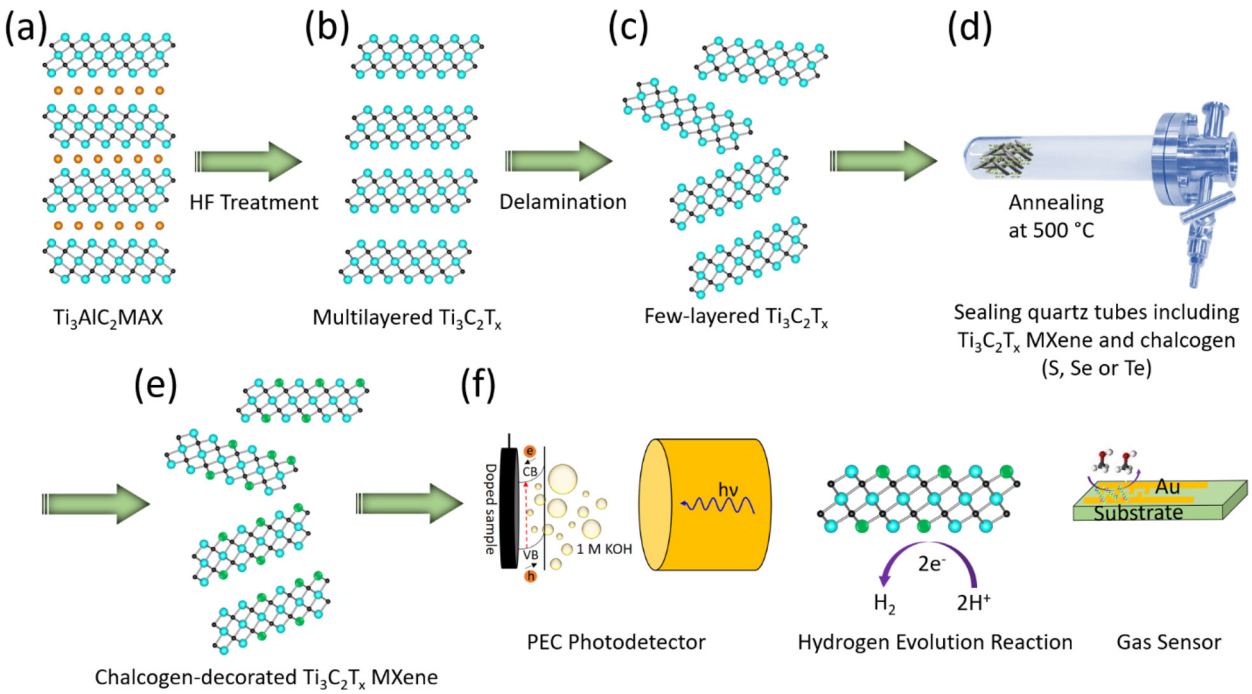

Scheme 1 A schematic illustration of the (a–e) step-by-step procedure for synthesizing few-layered $Ti_3C_2T_x$ and chalcogen decorated $Ti_3C_2T_x$ MXenes *via* HF etching, TBAOH, and solid-state annealing technique, respectively, and (f) applications of few-layered chalcogen decorated $Ti_3C_2T_x$ MXenes for PEC photodetector, HER, and gas sensors.

received Ti_3AlC_2 MAX phase material (Jinzhou Haixin Metal Materials, China) was initially immersed in 500 ml of hydrofluoric acid (40% HF, Sigma-Aldrich) solution and continually stirred under ambient conditions for 7 days. Then, the sample was detached through repeated rounds of centrifugation and re-dispersion in water until getting a neutral 7 pH value for the residual water. Thereafter, the obtained sample was kept in a vacuum oven set at 50 °C for complete drying. In the next step, 5 g of $Ti_3C_2T_x$ MXene was mixed with 250 mL of tetrabutylammonium hydroxide (40% TBAOH, Sigma-Aldrich) under ambient conditions for one hour. It was then ultrasonicated (~30 minutes, 400 W) at room temperature and separated by suction filtration, followed by washing with distilled water. Finally, the delaminated MXene was dried overnight in a vacuum oven set at 50 °C.

2.1.2. Synthesis of S-, Se- or Te-decorated few-layered $Ti_3C_2T_x$ MXene composites. The synthesized few-layered $Ti_3C_2T_x$ MXene (2 gr) and as-received chalcogen powders (S, Se, Te, 1 gr, 99.99% purity, Strem chemicals, Inc., USA) with the ratio of 2 MXene : 1 chalcogen were firstly weighed and inserted in a quartz glass ampule (Scheme 1d and e) and evacuated to 1×10^{-5} mbar with a diffusion pump and melt sealed. Following sealing with an oxygen–hydrogen torch, the quartz ampule was subsequently placed inside a muffle furnace and heated at 500 °C for 24 h using a 5 °C min^{-1} heating and cooling rate. Finally, the chalcogen decorated few-layered $Ti_3C_2T_x$ composite powders were manually collected from the broken quartz tube.

2.1.3. Preparation of working electrodes. To characterize the PEC photodetector, HER, and vapor sensing performances, indium tin oxide (ITO), glassy carbon (GC), and gold-interdigitated electrode (GIE) substrates were ultrasonically cleaned with acetone, ethanol, and deionized water and then dried by nitrogen flow. The surface of GC was also polished with a polishing kit including Al_2O_3 sol–gel suspension (Eposal, pH ~ 8.0, 0.06 micron) and polishing cloth (zeta, Ø = 200 nm, short-nap, soft synthetic cloth) to remove any contaminations prior to performing the ultrasonic cleansing. Then, 30 mg of each Ti_3AlC_2, few-layered $Ti_3C_2T_x$, and chalcogen decorated few-layered $Ti_3C_2T_x$ composite samples were dispersed in 1000 μl of *N*,*N*-dimethylformamide (DMF) using ice bath sonication for 15 min. Subsequently, 5 μl of each dispersed sample was uniformly drop-cast on ITO, GC, and GIE substrates (Scheme 1f) and dried in a vacuum oven at 65 °C for 12 h for further characterization.

2.2. Characterization methods

2.2.1. Materials characterization. The crystal structure of the synthesized materials was determined by X-ray diffraction (XRD, Bruker D8 Advance, Germany) equipped with a Cu-Kα (λ = 1.5406 Å) source, with 2θ degree values from 5 to 90°, and a step size of 0.02°. The morphology, microstructure, and elemental mapping of the materials were analyzed using a scanning electron microscope (SEM) and a transmission electron microscope (TEM, EFTEM Jeol 2200 FS microscope) equipped with an energy dispersive spectrometry (EDS) system with an acceleration voltage of 200 kV. SEM was also performed on Maia 3 and Lyra 3 (Tescan) in scanning transmission electron microscopy (STEM) mode for a better material contrast. X-ray photoelectron spectroscopy (XPS) analysis was performed *via* electron spectroscopy for chemical analysis with a Probe P spectrometer (Omicron Nanotechnology, Germany) using a monochromatized Al Kα X-ray source (1486.7 eV) to investigate the surface composition and bonding states. A LAMBDA 850 + UV/Vis Spectrophotometer (PerkinElmer, USA) inside the integration sphere with a scan range between 250 and 800 nm was used to carry out the UV-Vis spectroscopic characterization. To evaluate the specific surface area and pore size distribution of the synthesized materials, N_2 adsorption–desorption isotherms were analyzed at 77 K using a Quantachrome NOVAtouch LX^2. Before measuring gas sorption, the samples were activated at 150 °C for 10 hours under dynamic vacuum, with N_2 as the adsorbate.

2.2.2. Electrochemical characterization. PEC photodetection and HER electrochemical tests were carried out at room temperature in a three-electrode system with an Autolab PGSTAT 204 (Utrecht, Netherlands, NOVA Version 2.1.4). For the PEC photodetection and HER, drop-cast samples on ITO and GC substrates, respectively, were utilized as a working electrode, platinum (Pt) wire and graphite rod served as a counter electrode, and a Ag/AgCl/saturated KCl electrode served as a reference electrode. The CV scan range for the PEC photodetector was with a gate voltage from −0.5 to +0.5 V and a scan rate of 5 mV s^{-1}. However, that voltage range was changed from −1.5 to +2 V with the same scan rate for HER characterization. The HER and OER zones inside that particular characterization are denied due to the limited value of the scan range for the PEC photodetector. During the PEC photodetector characterization, we looked at illumination with several LED sources, ranging from 385 nm to 532 nm. Measurements with the PEC photodetector and the HER were carried out in 1 M KOH and 0.5 M H_2SO_4, respectively. An Auto lab (PGSTAT204) with the impedance module FRA32M was used to acquire and evaluate gas sensing in a two-electrode mode by impedance spectroscopy measurements at room temperature. The frequency range had a logarithmic scale of 10 points per decade and ranged from 0.01 Hz to 1 MHz.

3. Results and discussion

3.1. Crystal, morphological and chemical characterization

The crystal phases, structure, and morphology of the synthesized $Ti_3C_2T_x$ and chalcogen (S, Se, and Te) decorated few-layered $Ti_3C_2T_x$ MXenes (namely; Te/$Ti_3C_2T_x$, Se/$Ti_3C_2T_x$, and S/$Ti_3C_2T_x$) were characterized by XRD, SEM, and TEM/HRTEM. As depicted in the XRD characterization of Fig. 1, Aluminium (Al) layers of the Ti_3AlC_2 MAX phase were almost terminated after etching with 40% HF to gain the $Ti_3C_2T_x$ MXene. The obtained $Ti_3C_2T_x$ MXene also show a well-crystallized form. The critical heating temperature for the $Ti_3C_2T_x$ MXene chemi-

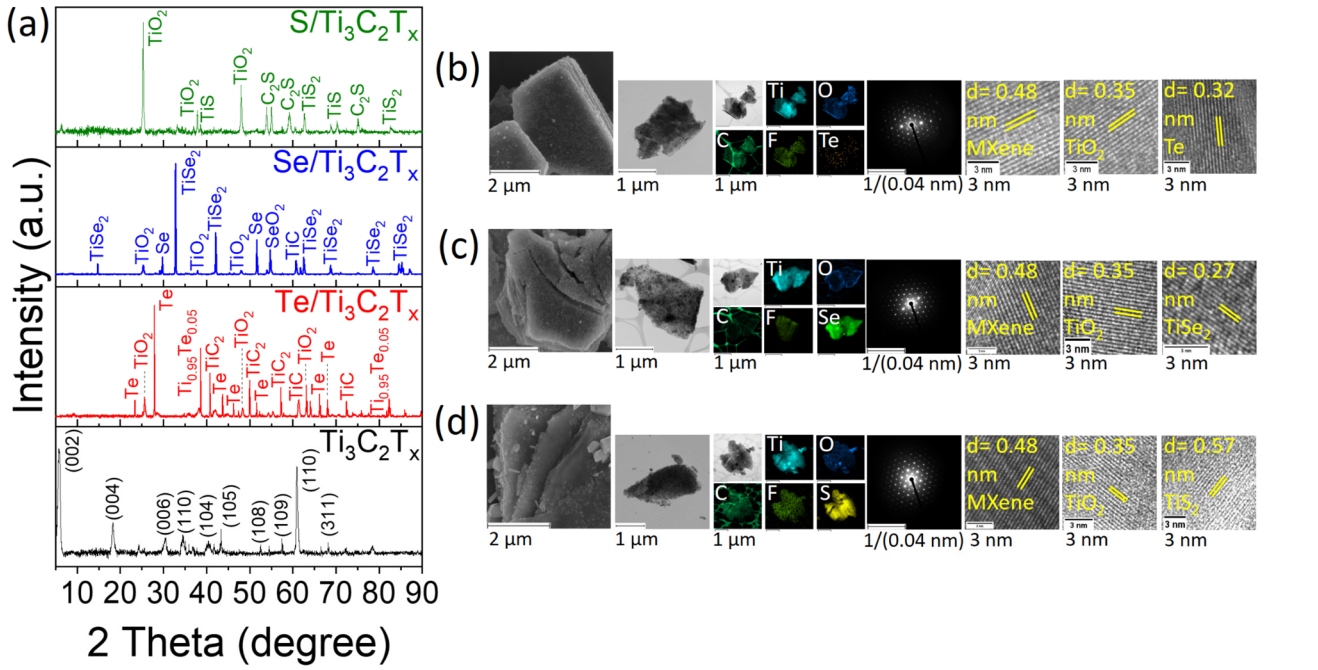

Fig. 1 Structural and morphological characterization of $Ti_3C_2T_x$, $Te/Ti_3C_2T_x$, $Se/Ti_3C_2T_x$, and $S/Ti_3C_2T_x$; (a) XRD, (b–d) typical SEM, TEM including elemental mappings, electron diffraction, and HRTEM of $Te/Ti_3C_2T_x$, $Se/Ti_3C_2T_x$, and $S/Ti_3C_2T_x$. (Note: the TEM and elemental mapping images of the synthesized $Ti_3C_2T_x$ have been provided in Fig. S1.†)

cal and structural phase transitions has been estimated to be around 850 °C.[30] Thus, a benign annealing temperature of 500 °C was implemented to just modify the surface chemistry and thermally break down the functional groups. Subsequently, it has been observed from the XRD patterns of $Te/Ti_3C_2T_x$, $Se/Ti_3C_2T_x$, and $S/Ti_3C_2T_x$ samples that the (002) and (004) peaks completely disappeared and were substituted by a group of sharp diffraction peaks that index mainly to Te and formed-$Ti_{0.95}Te_{0.05}$ (in $Te/Ti_3C_2T_x$), formed-$TiSe_2$ (in $Se/Ti_3C_2T_x$), formed-TiS_2 and TiS (in $S/Ti_3C_2T_x$), TiO_2 (in all samples), and some other compounds belonging to the Ti_3C_2 MXene and decorated chalcogen. It is hypothesized that a direct reaction between chalcogen elements and MXene layers which took place at 500 °C under vacuum conditions caused the majority formation of those chemical bonding and phases. The chemical reaction and bonding generally could be based on the fact that an atom from the surface functional groups (=O, –H, –OH, or –F) of the $Ti_3C_2T_x$ structure leaves its initial position (mostly –OH and some parts of –F)[30] at temperatures below the annealing's critical point, and then a vacancy is created that can be filled with chalcogen atoms and create covalent bonding with the nearby atoms. As a result, the elimination of –OH and maybe some portion of –F causes the formation of $Ti_{0.95}Te_{0.05}$, $TiSe_2$, TiS_2, and TiS on the surface of the MXene. A small degree of chemical reaction could be noticed between the Te chalcogen and $Ti_3C_2T_x$ MXene in the $Te/Ti_3C_2T_x$ sample. This low reaction of Te with MXene might be attributed to the high boiling point of Te (~988 °C) in comparison with the other S (~445 °C) and Se (~685 °C) chalcogen elements, where the annealing temperature applied at 500 °C is very less for a large chemical reaction for Te. The other formation phases of SeO_2 (in $Se/Ti_3C_2T_x$) and C_2S (in $S/Ti_3C_2T_x$) are also because of the existence of =O terminations on the MXene and the vacancy of Ti, respectively. The existence of the TiO_2 phase is also not astonishing because the annealed chalcogen decorated few-layered $Ti_3C_2T_x$ MXenes contained oxygen-containing species and a portion of –F surface terminations that are known to stabilize the TiO_2 anatase phase.[31,32] Regularly, the etching treatment procedure is frequently recognized to crumble the hexagonal crystal structure and *P*63/*mmc* symmetry of the MAX phase by elimination of A-layers. Nonetheless, the surface terminations on the MXene by intercalation of termination ions hold a portion of the hexagonal symmetry components of the parent MAX material. The SEM, TEM, electron diffraction pattern and HRTEM images of the synthesized $S/Ti_3C_2T_x$, $Se/Ti_3C_2T_x$, and $Te/Ti_3C_2T_x$ can confirm the structural stability of the $Ti_3C_2T_x$ MXene after annealing under vacuum conditions in the presence of the chalcogen decoration agents and also the formation of the aforementioned formed phases (Fig. 1b–d). These results of characterization are consistent with the XRD results that demonstrate the various morphologies formed in the chalcogen decorated few-layered $Ti_3C_2T_x$ MXene composite, without decomposition of the $Ti_3C_2T_x$ MXene support after annealing.

To further analyze the surface chemistry, chemical states, and atomic bonding configurations, the as-received Ti_3AlC_2 MAX and synthesized $Ti_3C_2T_x$, $Te/Ti_3C_2T_x$, $Se/Ti_3C_2T_x$, and $S/Ti_3C_2T_x$ MXenes were subjected to XPS characterization

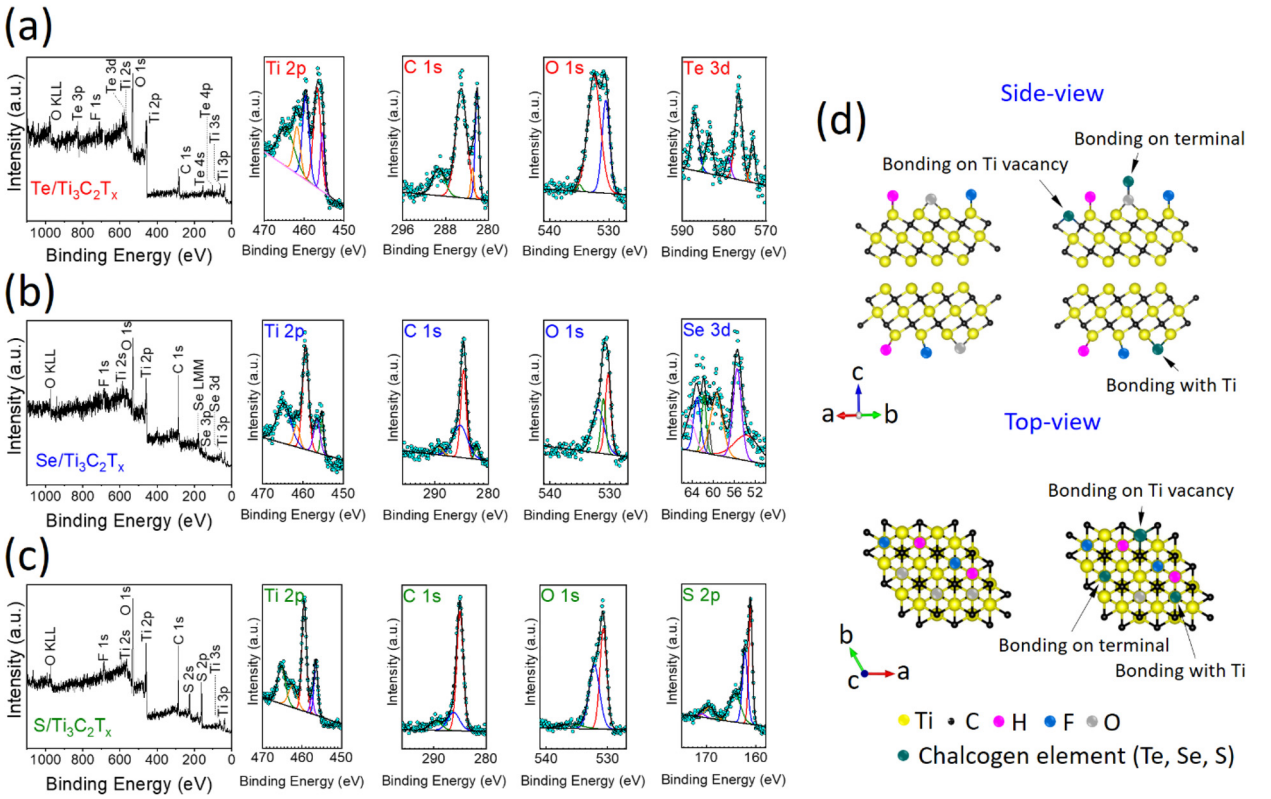

Fig. 2 XPS survey spectrum and high-resolution elemental spectra of (a) $Te/Ti_3C_2T_x$, (b) $Se/Ti_3C_2T_x$, and (c) $S/Ti_3C_2T_x$. (d) Schematic illustration of possible potential anchoring sites for the chalcogen decorated few-layered $Ti_3C_2T_x$ MXene composite (side- and top-view).

(Fig. S2† and Fig. 2a–c). The full XPS survey and high-resolution spectra could represent the distinct signals of Ti, C, O, F, S, Se, and Te elements. The samples' XPS analysis reveals that after annealing them with pre-selected chalcogen elements, the amount of F species significantly decreased while the content of O increased slightly. Similar results have been observed in single Se atoms on $Ti_3C_2T_x$ MXene nanosheets under CO_2 conditions,[26] as well as in our other recent work by the solid-state annealing method.[33] This variation would be due to the substitution in termination contents by chalcogen elements and oxygen-containing terminations (like Ti–O, C–O, S–O, and Se–O). High-resolution XPS spectra of the elements of the samples can further help evaluate the changes in chemical states and their occupancy after decoration of the few-layered $Ti_3C_2T_x$ MXene with Te, Se, and S (Fig. 2a–c). The Ti 2p peaks of the samples are devoted to certain bonds belonging to Ti–O (bond in TiO_2) and Ti–C (bond in $Ti_3C_2T_x$).[34,35] The C 1s and O 1s peaks are assigned to C–Ti, C–C, Se–C, S–C, C–O, and Ti–O bonds. In the XPS spectra of the Se 3d, S 2p, and Te 3d, peaks are ascribed to the anchoring of chalcogen elements on $Ti_3C_2T_x$.

There are three likely potential anchoring sites that could incorporate the chalcogen agent atoms to be bonded with the $Ti_3C_2T_x$ MXene (Fig. 2d). These three possibilities are: (i) bonding with the terminal groups on the surface and producing chalcogen–oxygen species, (ii) bonding with Ti atoms like surface terminals on $Ti_3C_2T_x$, and (iii) occupying the Ti vacancies that already have been created during the etching process of Ti_3AlC_2 MAX. The XRD and XPS analyses indicate that at a 500 °C annealing temperature under 10^{-5} mbar vacuum conditions, chalcogen atoms are prone to bond with any of those three alternatives. Formation of the $TiSe_2$, TiS, and TiS_2 phases in considerable quantities, however, supports the chemical bonding arrangement of Se and S with Ti. The nature of this chemical bonding is perhaps due to the leaving of the functional group components of –OH and –F at this annealing temperature and providing low formation energy for the formation of Ti–Se, Ti–S, and Ti–Te bonds. This situation could be observed as insignificant in the case of the Te chalcogen with the $Ti_3C_2T_x$ MXene maybe because of its high boiling temperature, and low thermal-annealing energy for the formation of chemical reaction bonding.

3.2. PEC photodetector

To discover the photoresponse performance of the chalcogen decorated few-layered $Ti_3C_2T_x$ MXene, the photocurrent density of the samples was examined and compared to those of the blank ITO substrate, as-received Ti_3AlC_2 MAX phase, and synthesized few-layered $Ti_3C_2T_x$ MXene. In this instance, a three-electrode setup was used to perform PEC characterization along with an appropriate sample dropped onto the conductive ITO wafer. Several LED light illumination of 420 nm,

460 nm, 385 nm, and 532 nm with a power of 800 mW were used to measure the dependence of the photocurrent on the wavelength. Fig. 3a depicts the representative potential–current density (*V–I*) curve for the synthesized few-layered $Ti_3C_2T_x$ MXene that was obtained using linear sweep voltammetry in 1 M KOH at a scan rate of 10 mV s^{-1}. It shows a distinct response to the 420 nm LED illumination when it is turned on and off along with a steady increase in current density against the evolution of the applied voltage.

The photocurrent density characterization of the ITO substrate, Ti_3AlC_2, and $Ti_3C_2T_x$ samples revealed very low to negligible current density ranges with 420 nm, 460 nm, and 532 nm illumination (Fig. S3†). Among the Ti_3AlC_2 and $Ti_3C_2T_x$ samples, the $Ti_3C_2T_x$ MXene illustrates a higher current density (1.2 μA cm^{-2}) than the Ti_3AlC_2 with only 0.3 μA cm^{-2} under the 420 nm illumination. Nevertheless, this current density value is still away from an arbitrary state. Besides, the current density of the $Ti_3C_2T_x$ MXene is also low under the other 460 nm (0.5 μA cm^{-2}) and 532 nm (0.4 μA cm^{-2}) illumination. Following that, the photocurrent activity of the chalcogen decorated $Ti_3C_2T_x$ composites was also evaluated. The collected results not only show an extraordinary photocurrent density of 12 μA cm^{-2} ($Te/Ti_3C_2T_x$ with 420 nm illumination), but also some other current density values were collected under 460 nm, 385 nm, and 532 nm illumination (Fig. 3b–d) which are almost equal to the maximum value of the $Ti_3C_2T_x$ sample under 420 nm. A steady stable state was observed in the current density of the chalcogen decorated few-layered $Ti_3C_2T_x$ composite samples with passing time. However, it can be seen that the current density value shows fluctuation in the blank few-layered $Ti_3C_2T_x$ sample with 460 nm and 532 nm LED lights. This achievement is probably due to the unstable condition of the sample on top of the ITO substrate. The value of response time, another important parameter in photodetectors, was determined on the representative $Te/Ti_3C_2T_x$ sample. The obtained results show a swift response and recovery time of ~1.0 s toward the illumination light (Fig. 4).

In order to gain further insight into the efficiency of the PEC photodetector, the responsivity (*R*) values of the $Ti_3C_2T_x$, $Te/Ti_3C_2T_x$, $Se/Ti_3C_2T_x$, and $S/Ti_3C_2T_x$ samples were assessed using $R = \frac{\Delta I}{P}$, where ΔI is the difference in the photocurrent density with respect to the dark current, and *P* is the irradiance power intensity per unit area (Fig. S4a† and Fig. 4a–c).[33]

It can be observed that the responsivity of the $Te/Ti_3C_2T_x$ sample (Fig. 5a) reaches 70 μA W^{-1} which is almost 20 times

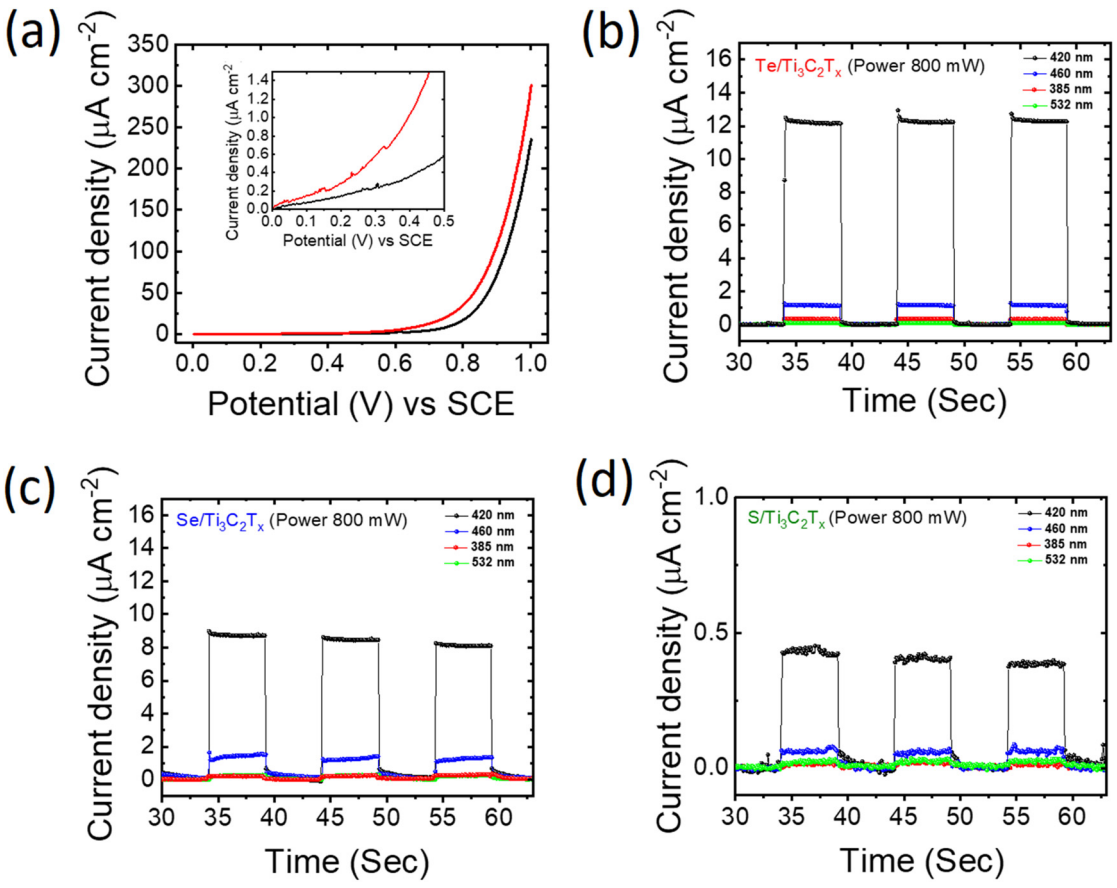

Fig. 3 (a) A representative anodic scan of a few-layered $Ti_3C_2T_x$ sample in 1 M KOH under 420 nm LED illumination. Photocurrent density of (b) $Te/Ti_3C_2T_x$, (c) $Se/Ti_3C_2T_x$, and (d) $S/Ti_3C_2T_x$ samples under the illumination of 420 nm, 460 nm, 385 nm, and 532 nm LED sources in 1 M KOH solution at 1.25 V *vs.* SCE.

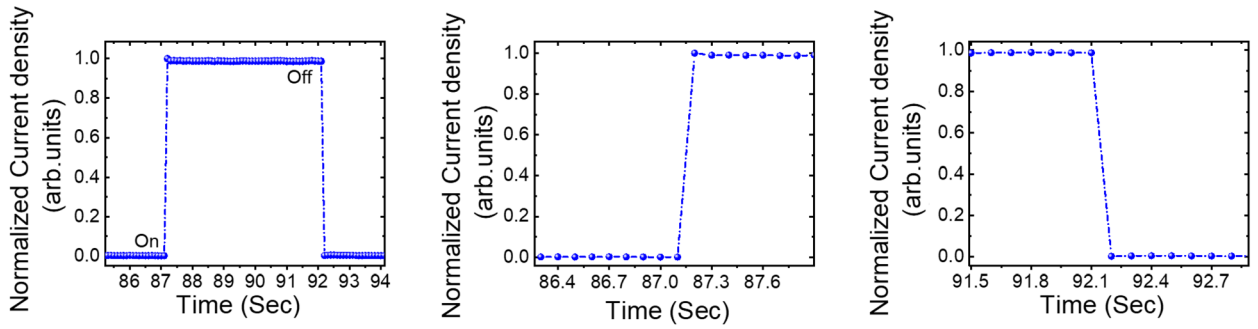

Fig. 4 A representative single-cycle response time, semi-cycle response, and recovery times of the PEC Te/$Ti_3C_2T_x$ photodetector in 1 M KOH solution under the 420 nm LED light with a power of 800 mW.

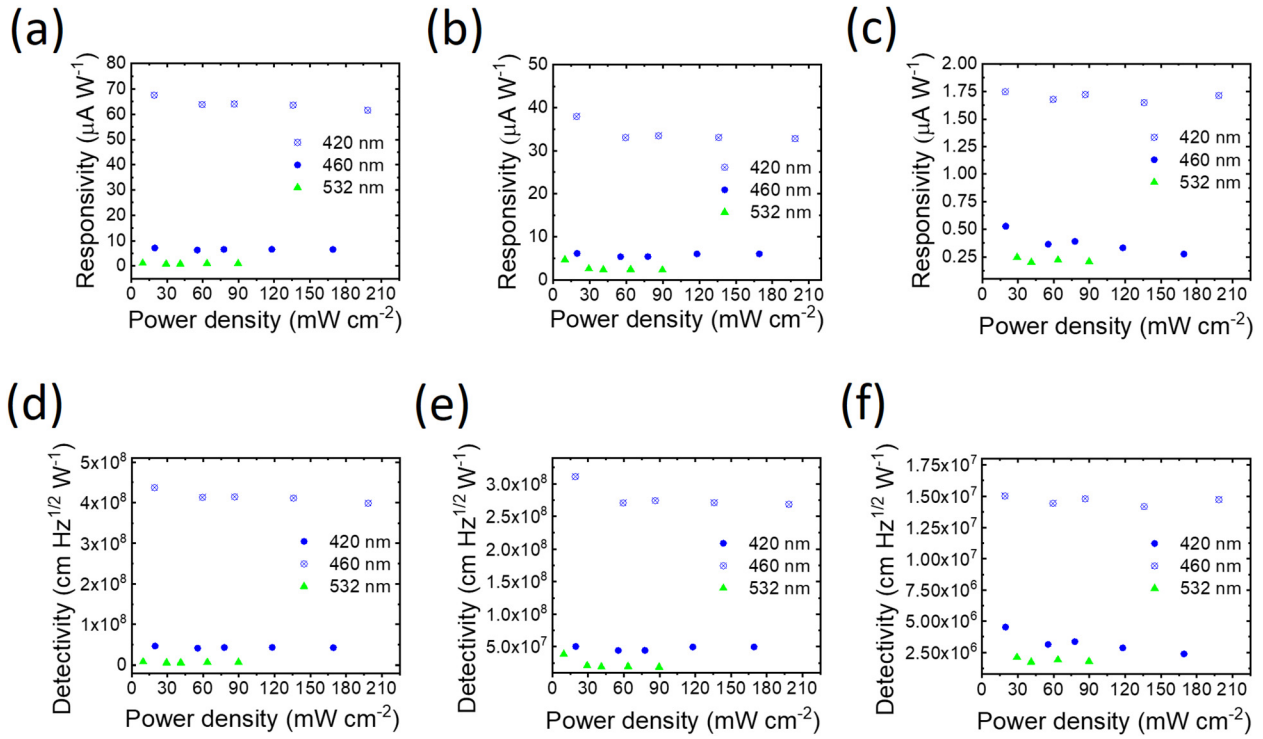

Fig. 5 The responsivity (a–c) and detectivity (d–f) of PEC Te/$Ti_3C_2T_x$, Se/$Ti_3C_2T_x$, and S/$Ti_3C_2T_x$ photodetectors, respectively, in 1 M KOH solution as a function of power density upon 420 nm, 460 nm, and 532 nm illumination wavelengths.

higher than the responsivity of blank few-layered $Ti_3C_2T_x$ (Fig. S4a†) and even possesses a higher value in comparison with the other Se/$Ti_3C_2T_x$ (Fig. 5b) and S/$Ti_3C_2T_x$ (Fig. 5c) samples. For further additional characterization, it is essential to evaluate the specific detectivity of a photodetector device which describes the minimum illumination power necessary for a photodetector to distinguish the signal from noise. Thus, the following formula is utilized to calculate the specific detectivity: $D^* = \frac{(AB)^{1/2}}{\mathrm{NEP}}$, where A and B represent the active area and measured bandwidth, respectively, and NEP represents noise-equivalent power.[36,37] NEP is defined as the input signal power that produces a signal-to-noise ratio (S/R) of one in an output bandwidth of 1 Hz. It also can be expressed as follows: $\mathrm{NEP} = \frac{I_N}{R_{ph}}$, where I_N is the noise current (dark current) and R_{ph} is the photodetector's photoresponsivity.[37] Fig. 4d–f display the detectivity of Te/$Ti_3C_2T_x$, Se/$Ti_3C_2T_x$, and S/$Ti_3C_2T_x$ samples, respectively. The maximum detectivity between the chalcogen decorated $Ti_3C_2T_x$ composite samples is likely due to the high carrier concentration at low dark current densities for the Te/$Ti_3C_2T_x$ sample with ~4.5 × 10^8 cm $Hz^{1/2}$ W^{-1} (Fig. 5d). The detectivity value for Se/$Ti_3C_2T_x$ and S/$Ti_3C_2T_x$ samples is ~3.0 × 10^8 cm $Hz^{1/2}$ W^{-1} and ~1.5 × 10^7 cm $Hz^{1/2}$ W^{-1}, respectively. On the other hand, the detectivity of the few-layered blank $Ti_3C_2T_x$ is ~1.2 × 10^7 cm $Hz^{1/2}$ W^{-1} (Fig. S4b†).

The low photodetection characteristic of the $Ti_3C_2T_x$ MXene could be attributed to the crystal defects which usually are formed on the $Ti_3C_2T_x$ MXene during the etching process of the Ti_3AlC_2 MAX phase. Those defects would represent a trap and then capture the photogenerated electron–hole pairs. On the other hand, the optical bandgap of the blank few-layered $Ti_3C_2T_x$ MXene has the highest value among the presented materials (Fig. 6a) of ~3.7 eV. This high value of the optical bandgap is due to the concentration of defects on the $Ti_3C_2T_x$ MXene, where the excess defect density shifts the Fermi level towards the conduction band, thereby giving rise to the Moss–Burstein effect and optical bandgap.[38] Hence, this high optical bandgap value of the $Ti_3C_2T_x$ MXene could be another possible reason for the lower performance in its photodetector activities. In the case of the chalcogen decorated few-layered $Ti_3C_2T_x$ MXene composite samples, those formation vacancies usually are occupied by the chalcogen elements. Therefore, photocurrent density could be developed in such decorated composite samples. Also, the optical bandgap of chalcogen decorated samples (Fig. 6a) declined to a lower value which has a beneficial effect on generation charge carriers and developing photocurrent density. The specific surface area of all samples also was analyzed using Brunauer–Emmett–Teller (BET) measurements. Fig. 6b shows that the surface area value of the $Ti_3C_2T_x$ MXene is lower than those of the other samples. This results in a low active surface area and subsequently, low charge carriers and photocurrent density for that sample. Although the surface area of $S/Ti_3C_2T_x$ is higher than those of the other two chalcogen decorated composite samples ($Te/Ti_3C_2T_x$ and $Se/Ti_3C_2T_x$), the higher photocurrent density of $Te/Ti_3C_2T_x$ is due to another physical phenomenon of ionization energy. One can speculate that an element with lower ionization energy can generate higher electron–hole pairs since the ionization energy is the minimum energy required to separate the most loosely bound electron. A comparison between the ionization energy of the chalcogen elements confirms that the ionization energy of Te is lower than those of the other two chalcogen elements (ionization energy: Te < Se < S).[39] This causes the enhancement of photocurrent density, photoresponsivity, and detectivity of $Te/Ti_3C_2T_x$ in comparison with the other $Se/Ti_3C_2T_x$ and $S/Ti_3C_2T_x$ samples. The formation of transition metal dichalcogenides on top of Se- and S-decorated $Ti_3C_2T_x$ MXenes in this work is the other possible reason for developing photodetection activities of the $Ti_3C_2T_x$ due to the high charge carrier mobility of those shaped phases.[40]

3.3. Hydrogen evolution reaction

The electrocatalytic efficiency of the chalcogen decorated $Ti_3C_2T_x$ MXene composite samples for the HER was evaluated by conducting linear sweep voltammetry (LSV) in an acidic environment (0.5 H_2SO_4). The achieved results were then compared with those of blank few-layered $Ti_3C_2T_x$ MXene, platinum–carbon (PtC, 1%), and GC substrate under the same experimental conditions to assess the origin of the developed HER performance of the chalcogen decorated influence on the $Ti_3C_2T_x$ MXene (Fig. 7). According to the typical overpotential value at a −10 mA cm^{-2} current density for the HER, the evalu-

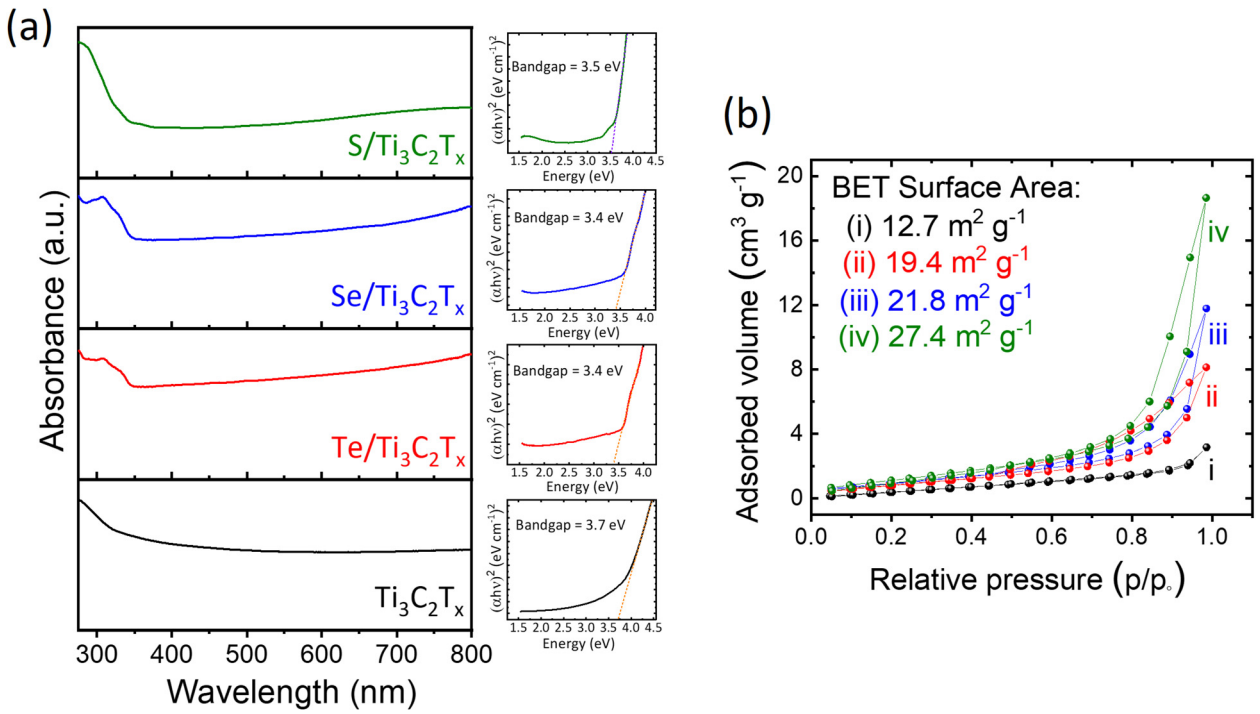

Fig. 6 (a) UV-Vis absorption spectra along with Tauc plots of the blank and chalcogen decorated $Ti_3C_2T_x$ composite samples. (b) BET analysis of (i) blank $Ti_3C_2T_x$ MXene, (ii) $Te/Ti_3C_2T_x$ (210 pm), (iii) $Se/Ti_3C_2T_x$ (190 pm), and (iv) $S/Ti_3C_2T_x$ (180 pm) samples.

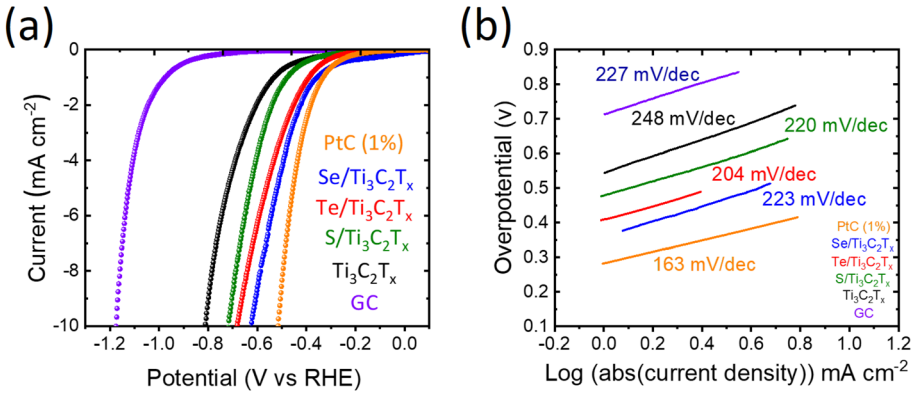

Fig. 7 HER analysis of the blank $Ti_3C_2T_x$ MXene, $Te/Ti_3C_2T_x$, $Se/Ti_3C_2T_x$, and $S/Ti_3C_2T_x$ samples in 0.5 M H_2SO_4 medium and compared with GC and PtC (1%) samples. (a) Polarization curves and (b) Tafel plots of the corresponding overpotentials.

ated overpotentials for the chalcogen decorated few-layered $Ti_3C_2T_x$ MXene composite samples illustrate an improvement in catalytic performance because of the new active sites as well as a newly formed phase by chalcogen decorated atoms. The Tafel analysis was also carried out to determine the electrochemical kinetics. Its slope identifies a logarithm of current density with overpotential and provides a simple way to recognize the rate-determining step, and hence, a possible electrochemical mechanism in the HER. It is observed from Fig. 7a that the $Se/Ti_3C_2T_x$ sample is willing to generate bonding sites with hydrogen atoms easier than the other measured samples. Generally, the possible mechanisms for the HER in acidic media could be based on the Volmer–Heyrovsky or Volmer–Tafel mechanism. The Volmer process always occurs at the initial step, and it is followed by either the Heyrovsky or Tafel process. However, one of Heyrovsky's or Tafel's actions would be as a predominant mechanism. For the Volmer step to be the rate-determining step, it already has been proven that the magnitude of the Tafel slope has to be around 120 mV dec^{-1}.[41,42] This value for the corresponding mechanisms of the Heyrovsky and Tafel step is observed at around 40 and 30 mV dec^{-1}, respectively.[41,43] The Tafel slopes for each sample were obtained from the linear portion of the polarization curves (Fig. 7b). It can be seen that the slope values are as follows: PtC 1% ~ 163 mV dec^{-1}, $Se/Ti_3C_2T_x$ ~ 223 mV dec^{-1}, $Te/Ti_3C_2T_x$ ~ 204 mV dec^{-1}, $S/Ti_3C_2T_x$ ~ 220 mV dec^{-1}, $Ti_3C_2T_x$ ~ 248 mV dec^{-1}, and GC ~ 227 mV dec^{-1}. According to the above explanations for the HER mechanism in acidic media and the acquired distinct Tafel slope values of the samples, it can be proposed that another different mechanism would occur for both blank and chalcogen decorated $Ti_3C_2T_x$ MXene composite samples that would be determined based on the following hypothesis. In the case of the blank $Ti_3C_2T_x$ MXene, oxygen (=O) terminal groups could be protonated with the existing high concentration of H^+ in the H_2SO_4 electrolyte resulting in Ti–OH bonding. This protonation could be followed by the adjacent Ti site and lead to the formation of H_2. Nonetheless, it is observed from Fig. 7b that the blank $Ti_3C_2T_x$ MXene suffers from a 248 mV dec^{-1} large overpotential value. This high overpotential value is maybe attributed to the lack of an ideal equilibrium between Ti and O sites in this sample.[44] In the case of the chalcogen decorated $Ti_3C_2T_x$ MXene composite samples, it already was proven by XPS characterization (Fig. S2† and Fig. 2) that the =O content was enhanced slightly after decoration. Therefore, this variation in the =O content legitimized the evolution of more H_2 contents in the modified samples. Likewise, the arrangement of $Ti_{0.95}Te_{0.05}$, $TiSe_2$, TiS, and TiS_2 phases in the chalcogen decorated $Ti_3C_2T_x$ composite samples is roughly unattainable to be stoichiometric, perhaps due to chalcogen vacancies.[45–47] The chalcogen vacancies and strain are also shown frequently to be the active sites in catalysts to maximize HER performance.[48–50] Also, the loss of chalcogen causes additional electrons to be redistributed among the nearby atoms.[51] As a result, the chalcogen vacancies at the surface of the chalcogen decorated $Ti_3C_2T_x$ composite sample may drive electron accumulation, which creates more active sites and speeds up the reaction rate of the H^+/e^- coupling and the generation of additional H_2 with a lowering overpotential value.

3.4. Vapor sensors

The improvement of cutting-edge gas sensor devices for tracking down a low-level density of volatile organic molecules is necessary. In this context, MXenes have been evaluated for gas sensors in view of their remarkable attributes, recently,[52–54] albeit the gas and vapor detection by MXenes has been viewed as more convoluted as opposed to the other 2D nanomaterials with surface adsorption and a regular charge movement.[55,56] This is maybe attributed to the layered accordion-like structure of MXenes, where the interlayers are able to swell and affect the gas response. To investigate the gas sensing efficiency of the chalcogen decorated few-layered $Ti_3C_2T_x$ MXene composites and compare it with the pristine $Ti_3C_2T_x$, herein, we used the electrochemical impedance spectroscopy strategy and evaluated the samples on some polar organic vapors of methanol, ethanol, and acetone. The detection of the gases by MXenes generally occurs based on the sensitivity level of the impedance signals derived from the variety of the local carrier on

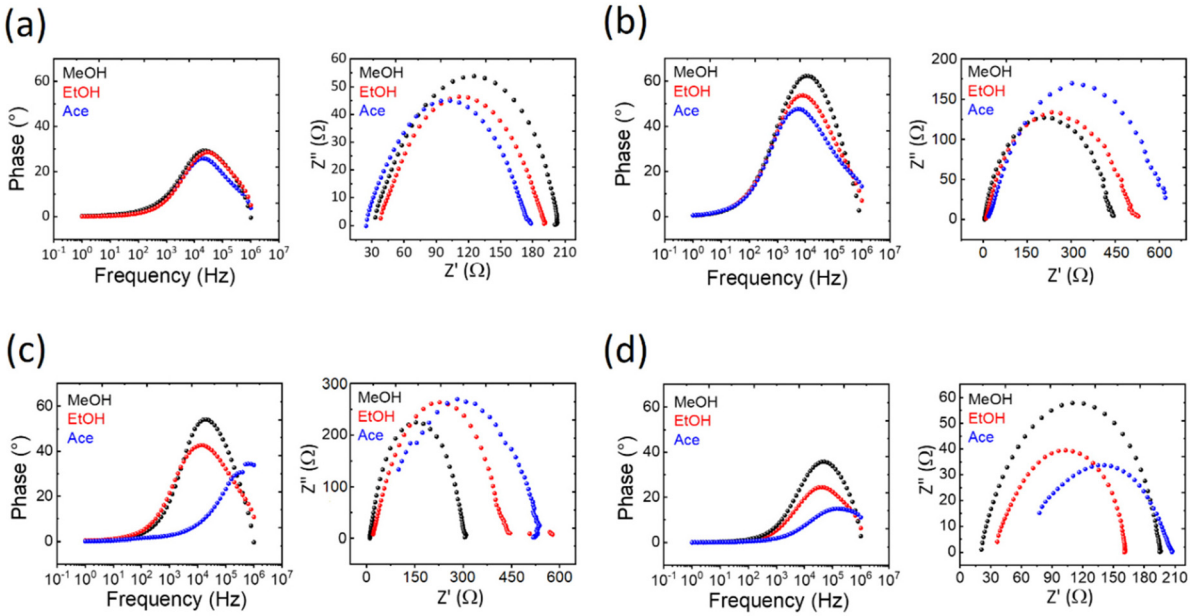

Fig. 8 Impedance phase spectra and Nyquist plots of the (a) pristine few-layered $Ti_3C_2T_x$ MXene, (b) Te/$Ti_3C_2T_x$, (c) Se/$Ti_3C_2T_x$, and (d) S/$Ti_3C_2T_x$ vapor sensors with methanol (MeOH), ethanol (EtOH) and acetone organic vapors.

the MXene layers. The Nyquist and Bode (impedance phase spectra) plots of the specimens are shown in Fig. 8. It can be observed from the Nyquist plots that all of the sample's behavior with the examined gases is like that of a series RC circuit. Also, it can be recognized that the resistance, combined capacitance, and inductance belonging to the real and imaginary sections of impedance (Z' and Z'') have been enhanced in the chalcogen decorated few-layered $Ti_3C_2T_x$ composite, especially for the Te/$Ti_3C_2T_x$ and Se/$Ti_3C_2T_x$ samples, in the presence of all vapors (Fig. 8). This Z' and Z'' increment could probably be due to the increased oxygen content, and subsequently, the formation of TiO_2 with an electrical resistivity of 10^{12} Ω cm^{-1},[57] as well as the other formed phases during decoration of $Ti_3C_2T_x$ with chalcogen elements. A comparison between the Bode phase plots of the pristine and chalcogen decorated few-layered $Ti_3C_2T_x$ composite samples indicates an enhanced affinity in the sensitivity of the Te/$Ti_3C_2T_x$ and Se/$Ti_3C_2T_x$ MXene samples. Amongst the latest two samples, Te/$Ti_3C_2T_x$ sensing performance seems to be even better maybe due to the less chemical reaction of Te with $Ti_3C_2T_x$. However, this trend is almost unchanged for the other S/$Ti_3C_2T_x$ in comparison with the pristine $Ti_3C_2T_x$. The sensing mechanism of chalcogen decorated $Ti_3C_2T_x$ composite samples with a positive variation could be discussed based on the following points of view: (i) the –F terminals with a detrimental effect on gas sensing have been reduced in chalcogen decorated $Ti_3C_2T_x$ samples.[55] (ii) The high polarity of the applied organic gases (methanol, ethanol, and acetone) and the interaction of those polar molecules with the enhanced =O terminals on the surface of the samples lead to charge transfer through the formation of hydrogen bonds. (iii) More electrons are produced on the surface of the chalcogen decorated $Ti_3C_2T_x$ composite samples as a result of the rich d-electrons of chalcogen elements and non-stoichiometric produced phases. This could increase the interaction of polar molecules with the sample and then enhance the extent of charge transfer. The suggested method for MXene anchoring components demonstrates that there are still areas that need to be thoroughly investigated while taking into account the manipulation of heterojunction interfaces and underlying gas-sensing processes.

4. Conclusions

MXenes have great potential to be used in a range of energy storage and energy conversion devices since they provide remarkable promise as photo(electro)catalysts. However, their efficiencies are yet to be developed with a few additional possible components and routes. As a result, some potential chalcogen elements of Te, Se, and S were selected and successfully anchored on the few-layered $Ti_3C_2T_x$ by a facile solid-state chemistry annealing technique. PEC photodetector, HER, and vapor sensor analyses revealed that the chalcogen decorated few-layered $Ti_3C_2T_x$ composite has a greater impact on the efficiencies of such systems than the pristine few-layered $Ti_3C_2T_x$ MXene. Occupation of pristine $Ti_3C_2T_x$ MXene defects and optical bandgap reduction by the chalcogen element decoration are two reasons for the enhancement of the photodetector activity of the chalcogen decorated $Ti_3C_2T_x$ MXene composite samples. Moreover, it was analyzed that the photocurrent density, photoresponsivity, and detectivity of Te/$Ti_3C_2T_x$ are higher than those of the other Se/$Ti_3C_2T_x$ and S/$Ti_3C_2T_x$ samples. This variation was due to the lower ionization energy of the Te in comparison with the other Se and S

elements. Thus, the Te/$Ti_3C_2T_x$ sample could transfer the separated electrons to the electrode system in the PEC photodetector more quickly and efficiently. The evaluation of the HER in the chalcogen decorated few-layered $Ti_3C_2T_x$ composite samples also showed an enhancement in the production of H_2 due to the large =O contents and non-stoichiometric formation phases on the surface of the $Ti_3C_2T_x$ MXene after modification. These two attributes could generate active sites to raise the H^+/e^- coupling reaction rate and form greater H_2. Furthermore, the reduced –F, higher =O, rich d-electron of chalcogen elements, and non-stoichiometric formed phases, all could boost electrons on the surface of the chalcogen decorated few-layered $Ti_3C_2T_x$ MXene composite samples, and subsequently, interactions by the methanol, ethanol, and acetone polar molecules with result in a larger charge transfer and vapor sensing. This work indicates an effective synthesis strategy in developing efficient materials for state-of-the-art applications and can provide new visions into the advancement of the other MXene-based family members that can be employed in high-performance energy systems.

Conflicts of interest

There are no conflicts to declare.

Acknowledgements

J. A. was supported by the European Structural and Investment Funds, OP RDE-funded project 'CHEMFELLS IV' (No. CZ.02.2.69/0.0/0.0/20_079/0017899). This project was supported by Czech Science Foundation (GACR No. 20-16124J).

References

1 X. Zhang, A. Chen, L. Chen and Z. Zhou, *Adv. Energy Mater.*, 2022, **12**, 2003841.
2 S. Khan, A. Khan, J. Azadmanjiri, P. Kumar Roy, L. Děkanovský, Z. Sofer and A. Numan, *Adv. Photonics Res.*, 2022, **3**, 2100342.
3 A. Khan, J. Azadmanjiri, B. Wu, L. Liping, Z. Sofer and J. Min, *Adv. Energy Mater.*, 2021, **11**, 2100451.
4 J. Zha, M. Luo, M. Ye, T. Ahmed, X. Yu, D.-H. Lien, Q. He, D. Lei, J. C. Ho, J. Bullock, K. B. Crozier and C. Tan, *Adv. Funct. Mater.*, 2022, **32**, 2111970.
5 J. Azadmanjiri, V. K. Srivastava, P. Kumar, J. Wang and A. Yu, *J. Mater. Chem. A*, 2018, **6**, 13509–13537.
6 P. K. Roy, N. Antonatos, T. Li, Y. Jing, J. Luxa, J. Azadmanjiri, P. Marvan, T. Heine and Z. Sofer, *ACS Appl. Mater. Interfaces*, 2023, **15**(1), 1859–1870.
7 M. Turunen, M. Brotons-Gisbert, Y. Dai, Y. Wang, E. Scerri, C. Bonato, K. D. Jöns, Z. Sun and B. D. Gerardot, *Nat. Rev. Phys.*, 2022, **4**, 219–236.
8 J. Azadmanjiri, V. K. Srivastava, P. Kumar, Z. Sofer, J. Min and J. Gong, *Appl. Mater. Today*, 2020, **19**, 100600.
9 S. Wei, S. Mourdikoudis, B. Wu, J. Pastika, R. Gusmão, J. Azadmanjiri, L. Dekanovsky, J. Luxa, M. Li and V. Mazánek, *2D Mater.*, 2022, **9**, 045032.
10 D. Zhao, Z. Chen, W. Yang, S. Liu, X. Zhang, Y. Yu, W.-C. Cheong, L. Zheng, F. Ren, G. Ying, X. Cao, D. Wang, Q. Peng, G. Wang and C. Chen, *J. Am. Chem. Soc.*, 2019, **141**, 4086–4093.
11 J. Zou, J. Wu, Y. Wang, F. Deng, J. Jiang, Y. Zhang, S. Liu, N. Li, H. Zhang, J. Yu, T. Zhai and H. N. Alshareef, *Chem. Soc. Rev.*, 2022, **51**, 2972–2990.
12 Y. Wang, T. Guo, Z. Tian, K. Bibi, Y.-Z. Zhang and H. N. Alshareef, *Adv. Mater.*, 2022, **34**, 2108560.
13 M. Zhang, C. Lai, B. Li, S. Liu, D. Huang, F. Xu, X. Liu, L. Qin, Y. Fu, L. Li, H. Yi and L. Chen, *Small*, 2021, **17**, 2007113.
14 A. Al-Temimy, B. Anasori, K. A. Mazzio, F. Kronast, M. Seredych, N. Kurra, M.-A. Mawass, S. Raoux, Y. Gogotsi and T. Petit, *J. Phys. Chem. C*, 2020, **124**, 5079–5086.
15 J. Xia, S.-Z. Yang, B. Wang, P. Wu, I. Popovs, H. Li, S. Irle, S. Dai and H. Zhu, *Nano Energy*, 2020, **72**, 104681.
16 L. Děkanovský, J. Azadmanjiri, M. Havlík, P. Bhupender, J. Šturala, V. Mazánek, A. Michalcová, L. Zeng, E. Olsson, B. Khezri and Z. Sofer, *Small Methods*, 2022, 2201329.
17 L. Gao, W. Bao, A. V. Kuklin, S. Mei, H. Zhang and H. Ågren, *Adv. Mater.*, 2021, **33**, 2004129.
18 M. Shekhirev, J. Busa, C. E. Shuck, A. Torres, S. Bagheri, A. Sinitskii and Y. Gogotsi, *ACS Nano*, 2022, **16**(9), 13695–13703.
19 K. R. G. Lim, M. Shekhirev, B. C. Wyatt, B. Anasori, Y. Gogotsi and Z. W. Seh, *Nat. Synth.*, 2022, **1**, 601–614.
20 L. H. Karlsson, J. Birch, J. Halim, M. W. Barsoum and P. O. Å. Persson, *Nano Lett.*, 2015, **15**, 4955–4960.
21 J. Azadmanjiri, T. N. Reddy, B. Khezri, L. Děkanovský, A. K. Parameswaran, B. Pal, S. Ashtiani, S. Wei and Z. Sofer, *J. Mater. Chem. A*, 2022, **10**, 4533–4557.
22 C. Zhang, Y. Ma, X. Zhang, S. Abdolhosseinzadeh, H. Sheng, W. Lan, A. Pakdel, J. Heier and F. Nüesch, *Energy Environ. Mater.*, 2020, **3**, 29–55.
23 A. Bafekry, C. V. Nguyen, C. Stampfl, B. Akgenc and M. Ghergherehchi, *Phys. Status Solidi B*, 2020, **257**, 2000343.
24 X. Li, X. Lv, X. Sun, C. Yang, Y.-Z. Zheng, L. Yang, S. Li and X. Tao, *Appl. Catal., B*, 2021, **284**, 119708.
25 X. Wu, Z. Wang, M. Yu, L. Xiu and J. Qiu, *Adv. Mater.*, 2017, **29**, 1607017.
26 D. Zhao, P. Wang, H. Di, P. Zhang, X. Hui and L. Yin, *Adv. Funct. Mater.*, 2021, **31**, 2010544.
27 J. Yao and G. Yang, *Adv. Sci.*, 2022, **9**, 2103036.
28 J. Azadmanjiri, L. Děkanovský, S. Wei, M. Li and Z. Sofer, *J. Energy Storage*, 2022, **56**, 105918.
29 H. L. Chia, C. C. Mayorga-Martinez, N. Antonatos, Z. Sofer, J. J. Gonzalez-Julian, R. D. Webster and M. Pumera, *Anal. Chem.*, 2020, **92**, 2452–2459.
30 M. Seredych, C. E. Shuck, D. Pinto, M. Alhabeb, E. Precetti, G. Deysher, B. Anasori, N. Kurra and Y. Gogotsi, *Chem. Mater.*, 2019, **31**, 3324–3332.

31 W.-J. Ong, L.-L. Tan, S.-P. Chai, S.-T. Yong and A. R. Mohamed, *Nanoscale*, 2014, **6**, 1946–2008.
32 M. Naguib, O. Mashtalir, M. R. Lukatskaya, B. Dyatkin, C. Zhang, V. Presser, Y. Gogotsi and M. W. Barsoum, *Chem. Commun.*, 2014, **50**, 7420–7423.
33 J. Azadmanjiri, P. K. Roy, L. Děkanovský, J. Regner and Z. Sofer, *2D Mater.*, 2022, **9**, 045019.
34 L. Zheng, S. Han, H. Liu, P. Yu and X. Fang, *Small*, 2016, **12**, 1527–1536.
35 C. Peng, P. Wei, X. Li, Y. Liu, Y. Cao, H. Wang, H. Yu, F. Peng, L. Zhang, B. Zhang and K. Lv, *Nano Energy*, 2018, **53**, 97–107.
36 M. Long, A. Gao, P. Wang, H. Xia, C. Ott, C. Pan, Y. Fu, E. Liu, X. Chen, W. Lu, T. Nilges, J. Xu, X. Wang, W. Hu and F. Miao, *Sci. Adv.*, 2017, **3**, e1700589.
37 P. K. Roy, P. Marvan, V. Mazánek, N. Antonatos, D. Bouša, E. Kovalska, D. Sedmidubský and Z. Sofer, *ACS Appl. Mater. Interfaces*, 2021, **13**, 30806–30817.
38 U. Bockelmann, P. Hiergeist, G. Abstreiter, G. Weimann and W. Schlapp, *Surf. Sci.*, 1990, **229**, 398–401.
39 P. Schwerdtfeger and J. K. Nagle, *Mol. Phys.*, 2019, **117**, 1200–1225.
40 T. S. Walmsley and Y.-Q. Xu, *Nanoscale*, 2021, **13**, 11836–11843.
41 A. P. Murthy, J. Theerthagiri, J. Madhavan and K. Murugan, *Phys. Chem. Chem. Phys.*, 2017, **19**, 1988–1998.
42 A. P. Murthy, J. Theerthagiri and J. Madhavan, *J. Phys. Chem. C*, 2018, **122**, 23943–23949.
43 H. Prats and K. Chan, *Phys. Chem. Chem. Phys.*, 2021, **23**, 27150–27158.
44 D. Johnson, H.-E. Lai, K. Hansen, P. B. Balbuena and A. Djire, *Nanoscale*, 2022, **14**, 5068–5078.
45 E. Mitterreiter, B. Schuler, A. Micevic, D. Hernangómez-Pérez, K. Barthelmi, K. A. Cochrane, J. Kiemle, F. Sigger, J. Klein, E. Wong, E. S. Barnard, K. Watanabe, T. Taniguchi, M. Lorke, F. Jahnke, J. J. Finley, A. M. Schwartzberg, D. Y. Qiu, S. Refaely-Abramson, A. W. Holleitner, A. Weber-Bargioni and C. Kastl, *Nat. Commun.*, 2021, **12**, 3822.
46 Y. Liu, P. Stradins and S.-H. Wei, *Angew. Chem., Int. Ed.*, 2016, **55**, 965–968.
47 K. Hu, L.-M. Guan, D. Han, F. Liu and S.-Y. Xie, *J. Phys. Chem. Lett.*, 2021, **12**, 9422–9428.
48 H. Li, C. Tsai, A. L. Koh, L. Cai, A. W. Contryman, A. H. Fragapane, J. Zhao, H. S. Han, H. C. Manoharan, F. Abild-Pedersen, J. K. Nørskov and X. Zheng, *Nat. Mater.*, 2016, **15**, 48–53.
49 H. Shu, D. Zhou, F. Li, D. Cao and X. Chen, *ACS Appl. Mater. Interfaces*, 2017, **9**, 42688–42698.
50 Y. S. Chang, C. Y. Chen, C. J. Ho, C. M. Cheng, H. R. Chen, T. Y. Fu, Y. T. Huang, S. W. Ke, H. Y. Du, K. Y. Lee, L. C. Chao, L. C. Chen, K. H. Chen, Y. W. Chu and R. S. Chen, *Nano Energy*, 2021, **84**, 105922.
51 M. Wang, Z. Sun, H. Ci, Z. Shi, L. Shen, C. Wei, Y. Ding, X. Yang and J. Sun, *Angew. Chem., Int. Ed.*, 2021, **60**, 24558–24565.
52 S. M. Majhi, A. Ali, Y. E. Greish, H. F. El-Maghraby, N. N. Qamhieh, A. R. Hajamohideen and S. T. Mahmoud, *ACS Appl. Electron. Mater.*, 2022, **4**(8), 4094–4103.
53 J. Lee, Y. C. Kang, C. M. Koo and S. J. Kim, *ACS Appl. Nano Mater.*, 2022, **5**(8), 11997–12005.
54 J. Choi, B. Chacon, H. Park, K. Hantanasirisakul, T. Kim, K. Shevchuk, J. Lee, H. Kang, S.-Y. Cho, J. Kim, Y. Gogotsi, S. J. Kim and H.-T. Jung, *ACS Sens.*, 2022, **7**(8), 2225–2234.
55 S. Mehdi Aghaei, A. Aasi and B. Panchapakesan, *ACS Omega*, 2021, **6**, 2450–2461.
56 R. Bhardwaj and A. Hazra, *J. Mater. Chem. C*, 2021, **9**, 15735–15754.
57 X. Mettan, J. Jaćimović, O. S. Barišić, A. Pisoni, I. Batistić, E. Horváth, S. Brown, L. Rossi, P. Szirmai, B. Farkas, H. Berger and L. Forró, *Commun. Phys.*, 2019, **2**, 123.